PCCP

Accepted Manuscript

ROYAL SOCIETY OF CHEMISTRY

www.rsc.org/pccp

Physical Chemistry Chemical Physics

ARTICLE

The use of multiple pseudo-physiological solutions to simulate the degradation behavior of pure iron as metallic resorbable implants: A surface-characterization study

Received 00th January 20xx,
Accepted 00th January 20xx

DOI: 10.1039/x0xx00000x

www.rsc.org/

Ranna Tolouei[a], Jerome Harrison[a], Carlo Paternoster[a], Stephane Turgeon[a], Pascale Chevallier[a], Diego Mantovani[a,†]

Understanding the interactions of the pure iron surface with biological elements, such as ions and proteins in an aqueous medium, is essential for an accurate in-vitro assessment of corrosion patterns. In fact, the synergy of chlorides, carbonates, phosphates and complex organic molecules present in body environment is a key factor affecting both in-vivo and in-vitro degradation of materials and especially for iron and its alloys. The aim of this work was the assessment of degradation patterns of pure iron in 5 commercial pseudo-physiological solutions by a thorough study of degraded surface chemistry and morphology. It also provides a methodological basis to understand the short-term degradation mechanism of degradable iron depending on the surrounding physiological media. The standard static immersion corrosion test was modified to adapt the procedure to pseudo-physiological solutions. After a 14-day static immersion test, the surfaces of samples were investigated by scanning electron microscopy, stylus profilometry and atomic force microscopy techniques. Chemistry and phase composition of the degraded layers were evaluated respectively by X-ray photoelectron spectrometry and X-ray diffractometry. Morphology and composition of the degradation layers were found to be different for the test- solutions: for phosphate-rich solutions, the formation of an adherent passive layer was found; degradation mechanisms related to general corrosion were predominant for all the other solutions. In conclusion, the chemical composition of the used medium plays a fundamental role in the degradation pattern of pure iron, so that direct comparisons of solutions with different ion concentration, as reported in the literature, need to be carefully assessed.

Introduction

In the last decades, biomaterials and implants saved the life or improved its quality for millions around the globe. Thus far, only corrosion-resistant (permanent biomaterials) are used clinically. Since 2004, a new class of temporary implants is clinically envisioned, and new resorbable metals engineered, included magnesium (Mg) and its alloys, iron (Fe) and its alloys as well as zinc (Zn) and its alloys. Metallic resorbable implants are expected to support mechanically the healing process of host tissue for a limited time and, therefore, to degrade into the human body without compromising its vital functions.[1] An ideal metallic resorbable implant would have a controllable degradation rate but would also conserve its mechanical integrity during surrounding tissue regeneration period. A uniform degradation is desired since inhomogeneous corrosion could cause mechanical failure of the device which would be catastrophic, especially in first stages of the healing process.[2] In addition, it is important to investigate not only the biocompatibility of the material but also the biocompatibility of the degradation products.

Short-term[3] and long-term[4] follow-up investigation of pure iron stents in porcine coronary arteries revealed safety and proved the in-vivo degradation behaviour of the material. Results of a 52-week study of a pure iron pin in a rat femoral bone demonstrated no sign of local or systematic toxicity as well as "a relatively slow degradation".[5] Despite remarkable advances in resorbable biomaterials testing, there is a noticeable difference between the corrosion rate of pure iron measured in-vitro, by standard immersion tests (~ 0.2 mm y^{-1}), and that observed in-vivo (negligible and not quantifiable).[5] These differences might be attributed to the fact that a simple static immersion test cannot mimic the complex physiological environment in which biomaterials would be placed; that is responsible for intricate degradation patterns through interactions with proteins, bicarbonates, aggressive ions and surrounding living tissues.

Furthermore, Pierson *et al.* reported that pure iron wires experienced degradation in different ways when implanted in rat abdominal aorta wall or its lumen. Ion-rich blood environment forms a phosphate layer on the metallic surface thus hindering the corrosion of wires, whereas wires in the aorta wall may passivate to a lesser extent.[6] It concluded that

[a] *Laboratory for Biomaterials and Bioengineering, CRC-I, Department of Mining, Metallurgical and Materials Engineering & CHU de Quebec Research Centre, Laval University, Quebec City, Canada.*
† Contact author: Diego Mantovani, PhD, FBSE, Laval University, Pavilion Adrien-Pouliot, 1065 Ave de la Médecine, Québec (QC), Canada G1V 0A6; Tel: +1 418 656 2131x6270 Fax: +1 418 656 5343; E-mail: Diego.Mantovani@gmn.ulaval.ca

dissimilar behaviours of implanted iron wires depended on the test environment with different chemical compositions.

Research on the degradation of iron and iron-based alloys for resorbable implants in cardiovascular and orthopaedic applications was done sporadically. Various methods were employed to increase the corrosion rate of iron implants, such as incorporation of alloying elements to the base materials[5, 7, 8] and fabrication of iron tubes by electroforming process.[9] These approaches are promising since the calculated corrosion rates in all cases resulted higher than that of the pure iron. In a recent review by Francis *et al.*, acellular in vitro behaviour of iron and iron-based alloys resulted to be heavily affected by the processing techniques.[10] They reported the corrosion rates of different iron-based samples in different pseudo-physiological solutions and concluded that electroformed pure iron possesses the highest one. Despite a great deal of data available in the literature, many parameters concerning the details of the experimental setup (i.e. ionic composition of solutions) are omitted or varied and general term of Hanks' or simulated body fluid (SBF) solution were reported.[10-12] However, degradation of iron and formation of degradation products in a saline solution with a CO_2-rich atmosphere (as in human blood plasma) is a complex phenomenon susceptible also to ion concentration of test solution. Since corrosion patterns are greatly affected by experimental parameters, a direct comparison between the reported researches can also be ambiguous or impossible.

The aim of the current work was to highlight the multi-facet degradation behaviour of pure iron as a function of the composition of test-solution on the basis of standard static immersion test, ASTM G31. In particular, five common commercial pseudo-physiological media were selected to evaluate the influence of ions combined interactions on pure iron degradation under a controlled CO_2-rich atmosphere. Degradation behaviour of pure iron was studied by characterization of the sample surfaces and the degradation products. This approach would provide the background for the harmonization of the current standards. At the same time, it would be a useful methodology for development of iron-based alloys for the metallic resorbable medical device. It could also offer a rather complete approach to filling the gap between in-vivo and in-vitro test results by assessing the single and synergetic effects of ions and complex molecules (proteins, glucose, etc.).

Materials and Methods

2.1 Material preparation

Specimens from Armco® iron sheet (Goodfellow, 99.5 wt. % Fe as-rolled sheet, impurities in ppm: Mn ~3000, Si ~1000, C <800, P <400, S <500) were cut. The 2-mm thick sheet was cold rolled until it reached a thickness of 0.4 mm, then it was thermally treated (1 hour at 550 °C, 10 °C/min) in controlled atmosphere (10% H_2, 90% Ar, AirLiquide, 99.99% pure) and cooled in the furnace; then 20 × 10 mm² samples were cut and a 1.1 mm diameter hole was drilled; this feature was used for the degradation test as described in *ASTM G31-03*. Before the degradation test, samples were ground and polished, with 240–4000 SiC papers, until a mirror finish observed.

2.2 In vitro test

Static immersion degradation tests were realized accordingly to *ASTM G31-03* Standard. Five common pseudo-physiological solutions were selected for a 14-day test in a controlled atmosphere incubator (T= 37.0 ± 1 °C, $p_{rel.\ CO2}$ = 5% and 90% of humidity); 1: A saline solution (NCS) was prepared with 8.94 g of NaCl (S5886-1KG, Sigma-Aldrich) in 1L of nanopure water, 2: Commercial Hanks' balanced salt solution (CHBS) was prepared with 9.5 g of balanced Hanks' salts (H2387, Sigma-Aldrich) in 1 L of nanopure water, 3: Modified Hanks' balanced salt solution (MHBS) was prepared with 9.7 g of balanced Hanks' salts (H1387, Sigma-Aldrich), 3.3 g of $NaHCO_3$ (S8875-500G, Sigma-Aldrich), 14.1 g of HEPES acid (H3375-500G, Sigma-Aldrich), 16.6 g of HEPES-Na salt (H7006-500G, Sigma-Aldrich) in 1.4 L of nanopure water, 4: Dulbecco's phosphate buffered saline (DPBS) was prepared by dissolving 9.6 g of Dulbecco's phosphate buffered saline salts (D5652, Sigma-Aldrich) in 1 L of nanopure water, 5: Dulbecco's phosphate buffered saline with albumin (APBS) was prepared by adding 1 g of bovine serum albumin (BSA) (A2153-50G, Sigma-Aldrich) to DPBS. The ionic compositions of the solutions as compared to that of human plasma are presented in Table 1. The pH of all the solutions was measured and adjusted to 7.4 by using 1M NaOH or HCl aqueous solutions; pH of APBS was adjusted before albumin addition. Afterwards, solutions were sterilized by filtration under a biological hood with a Steritop® vacuum-driven disposable filtration system (SCGPS02RE, EMD Millipore, USA).

Sample preparation was performed in a biological hood in sterile conditions; glassware and tools were autoclave-sterilized (T=121 °C, p=15 psi for 15 min). Immediately before sample immersion, samples were subjected to 1h UV sterilization under the hood. Pyrex bottles (100 mL, 1395-100 Corning Inc.) were filled with 95 mL of solution, and samples were immersed. A minimum ratio of test solution volume to test specimen surface area of 0.2 mL mm^{-2} should be respected according to the ASTM G31. After the test, samples were rinsed with ethanol and were stored in a vacuum desiccator (Vacuum Oven Model 29) at the room temperature until further use.

Afterward, the solution was collected from the test bottles, to extract solid degradation products formed during the test by centrifugation (at 4000 rpm with the centrifugal force of approximately 1.3 N, CS-6R Beckman, Canada).

2.3 Sample characterization

X-Ray diffraction (XRD) characterization was performed by a Siemens D5000 diffractometer equipped with a Cu tube ($\lambda_{K\alpha1}$ = 1.54060 nm) at a scanning rate of 0.02°/1.2 s^{-1} in the 2θ range 5 - 70°; the diffractometer was operated at 30 mA and 40 kV and equipped with a curved graphite crystal monochromator. X-ray photoelectron spectroscopy (XPS) measurements were carried out to investigate the chemical composition of the surface of degraded samples (PHI 5600-ci spectrometer,

Physical Electronics U.S.A), with an incident angle of 45° with the respect to the surface, normal and a residual pressure of 5×10^{-9} torr. A survey spectrum was first recorded using a standard aluminum X-ray source for survey spectra (0-1400 eV) at 200 W to identify all elements presents at the surface. High-resolution spectra (HR) of C1s, O1s and $Fe2p_{3/2}$ regions were recorded with a standard magnesium K_α X-ray source (1253.6 eV) at 150 W. The spectrometer work function was adjusted to give 285.0 eV for the main C1s peak. Curves fittings were determined using Gaussian-Lorentzian (80-20) function and a Shirley-type background and performed by the software Multipack®. The high resolution (HR) spectra for the O1s region have been obtained for all samples. Each oxygen peak was decomposed into three Gaussian/Laurentian components which have been attributed to the presence of metal oxides, hydroxides/phosphates, and carbonates/water. Tabulated XPS data were used to investigate the peak position related to oxygen and oxygen compounds on the XPS spectra (Table 2).

A JEOL JSM-840A, equipped with a tungsten filament and operated with an acceleration voltage of 15 kV, was used for scanning electron microscopy (SEM) and electron dispersive X-ray spectrometry (EDS) analyses. Micrographs were acquired with a probe current in the range 1×10^{-10} - 1×10^{-8} mA, while EDS spectra were acquired with a probe current of 1×10^{-8} mA, through a Ge detector (Nolan) whose resolution was 115 eV. Acquisition time for each spectrum was 60 sec.

After the in-vitro test, the topography and roughness of the samples were measured using a surface profilometer (DektakXT, Bruker) and an atomic force microscopy (AFM), respectively. A force of 3 mg was applied on the 12.5 µm radius stylus tip of the profilometer to limit the damage to the sample surfaces. AFM investigations were performed using the tapping mode of a Dimensions™ 3100 atomic force microscope (Digital Instruments, Bruker) with an etched silicon tip (model NCHV, tip radius 40 nm, Bruker). Surface topography was evaluated by profilometry for different surface areas, and the surface roughness was evaluated using profile (2D) parameters and surface (3D) parameters models. Indexes, principal, and geometrical content are similar for both cases. However, 2D parameters are described by functions of one variable (e.g. Eq. 1) while 3D parameters are characterized by functions of two variables. Considering the spatial topography (e.g. Eq. 2), 3D parameters provide more detailed and richer information.[13]

$$R_a = \frac{1}{l}\int_0^l |Z(x)|\, dx \qquad \text{Eq. 1}$$

$$S_a = \frac{1}{A}\iint_A |Z(x,y)|\, dxdy \qquad \text{Eq. 2}$$

where, R_a is the arithmetic mean height value of profile roughness, and Sa is the arithmetic mean height value of spatial roughness.

Results

3.1. Surface chemical properties

X-ray diffraction analysis of the samples shown in Fig. 1 identifies different phases on the degraded surfaces when exposed to multiple pseudo-physiological media. The main peak of diffraction patterns are entirely consistent and correspond to α-Fe (JCPDS card No. 06-0696) compatible to as-received pure iron.

Fig. 1a shows the corresponding peaks to magnetite (Fe_3O_4) for the sample immersed in NCS, with characteristic peaks at 30.1° (220), 35.5° (311), 43.1° (400), 53.4° (422), 57.0° (511) and 62.6° (440), according to JCPDS card No. 19-0629 and no other phase were detected. The XRD pattern of the sample immersed in CHBS is nearly identical to that of pure iron indicating that no significant degradation product or layer could be detected in the material. The diffraction peak at 15° for the sample immersed in MHBS can be confidently indexed as the (200) reflection of the γ-FeOOH (JCPDS card No. 44-1415).

The XRD pattern of the sample immersed in DPBS indicates that the surface has been covered by β-FeOOH (JCPDS card No. 34-1266), ferrous phosphate ($Fe(H_2PO_4)_3.2H_2O$) (JCPDS card No. 43-0104) and/or $Fe_3(PO_4)_2{\cdot}8H_2O$ (vivianite) (JCPDS card No. 30-0662). A poorly crystalline pattern showing only one angle reflection around 29° has been observed for the sample immersed in APBS, which could be attributed to amorphous ferrous phosphate degradation layer. The influence of protein addition to DPBS solution will be further investigated through XPS analysis and microscopic observations.

Degradation products of the samples immersed in CHBS, MHBS and NCS are poorly adherent, their flaking exacerbating the degradation process. The phase compositions of the loosed degradation products collected from the bottom of test bottles are shown in Fig. 1b. A mixture of α-FeOOH and γ-FeOOH powders was found for the samples immersed in CHBS and MHBS, while, degradation product powder from samples immersed in NCS showed a mixture of γ-FeOOH and Fe_3O_4. On the contrary, the layers of degradation products on the samples immersed in PBS and APBS are compact and adherent.

The survey spectra reveal characteristic peaks assigned to iron (Fe2p), oxygen (O1s) and carbon (C1s) photoelectrons, for all the samples. The surface of as-received samples revealed a higher carbon content, indicating that the cleaning process did not completely remove contaminations from the surface while after the degradation test, a reduction in the carbon content and a relative increase of oxygen was detected. These variations may be related to the replacement of the original surface by degradation products which are less enriched in C-C/C-H groups.

Analysis of survey spectra after in vitro test indicated the presence of nitrogen (N1s) only on the sample immersed in APBS, which is also evidenced by higher C1s content as compared to the sample immersed in DPBS. Nitrogen might be attributed to amine and amide groups in protein molecule that could confirm the adsorption of protein on the topmost layer during the degradation of the sample immersed in APBS.

As expected from Table 1, the presence of sodium, calcium, phosphorus and sulphur on the surface of samples immersed

in MHBS and also the presence of chloride ions on the surface of samples immersed in CHBS, MHBS and NCS were observed.

The HR-O1s peak of samples has been fitted with three peaks (Table 2): O1s(1) at a binding energy of 530.0 eV assigned to Fe-O, O1s(2) at a binding energy of 531.6 eV assigned to Fe-OH/Fe-PO_4 and O1s(3) at a binding energy of 533.0 eV assigned to Fe-CO_3/H_2O [14-20]. An analysis of the O1s spectra, listed in Table 3, revealed an increase in iron hydroxide/phosphate for the sample immersed in CHBS as compared to the samples immersed in MHBS and NCS. It also shows an increase of iron-oxide for the sample immersed in NCS compared to that of the samples immersed in CHBS and MHBS. The sample immersed in CHBS clearly display the existence of ferrous hydroxide and ferrous oxide on the surface, while as seen in Fig. 1, the XRD pattern of the sample showed no phase other than α-Fe. That discrepancy could be due to the thinner thickness of degradation products layer on this sample.

Considering the complex nature of oxidation/precipitation on iron surfaces, the fitting of multiple iron species is challenging. Unreliable interpretation can be produced for the speciation of iron surface chemical state due to many possible iron species with overlapping binding energies.[21]

3.2 Surface Microstructure

The surface of pure iron samples exposed for two weeks to NCS, CHBS and MHBS are bright silver. The samples immersed in CHBS and MHBS also covered with yellow-orange colour spots which are prone to flake off. In the case of NCS solution, the samples were also covered by dark spots (which could be attributed to the formation of Fe_3O_4). On the other hand, the surfaces of pure iron samples immersed in DPBS and APBS were dark blue grey which is ascribed to the formation of an iron phosphate coating. To assess the various growth mechanisms of degradation layer, the morphologies and microstructure evolutions of the immersed samples were observed and characterized by SEM, DEKTAK and AFM techniques as depicted in Fig. 2 and Table 4.

SEM images of the surface of samples immersed in DPBS and APBS show that albumin influences the formation of degradation layer by reducing the number of beads while increasing their size. The samples' surface displayed spherical shapes precipitations with featureless morphology (an indication of amorphous structure), and the diameters of the particles were in the range of 1-2 µm. The presence of organic compounds (protein) played the role of nucleation inhibitor in the precipitation process. It has been shown in the literature that the presence of proteins affects the crystallinity and the shape of the phosphate aggregates on a surface.[22, 23] EDS spectra indicated that the degradation product layers over samples immersed in phosphate contain solution contain P, O, Na and Fe, which indicated the formation of iron phosphorus compounds. The presences of cracks suggest a dehydration of the layer when removed from the solution and air-dried. However, trenches seem to be narrower on the surface of samples immersed in PBSA solution.

The SEM images of the surface of samples immersed in NCS revealed a porous surface and parts with similar morphology as of the surface of samples immersed in CHBS and MHBS solutions. The general view of the samples surface immersed in CHBS and MHBS (Fig. 2) are rough and associated with relatively coarse transgranular degraded surfaces; this revealed a specific crystallographic configuration of the degraded grains facets and steps. During the in-vitro test, the selective grain orientation-dependent dissolution behavior of samples results in the retraction of the {001}, {011} and {111} grains that are composed of a number of facets with different heights (Fig. 3).

AFM images of the samples after the 14-day in vitro test are also shown in Fig. 2. Due to different characteristics of the surfaces, it was essential to capture AFM images with dissimilar scan size. Remarkably, images demonstrate the same morphologies as seen through SEM images of samples surface immersed in CHBS, MHBS and NCS. As measured by AFM images the height of facet on the {111} grain is in the range of 100 to 250 nm while the step height on the {001} grain is the range of 50 to 100 nm. While upon exposing the samples to APBS and PBS, deposition of uniform layer occurred on the surface. Particularly, the surface of the beads on the sample immersed in APBS is smoother (R_q < 10 nm), larger in diameter (~800 nm) and lower in height (<200 nm) as compared to the ones for the sample immersed in PBS (R_q > 20 nm, 250 nm of diameter and >500 nm height).

Table 4 presented the comparison between 2D and 3D surface texture parameters measured by DEKTAK for the surfaces of samples after the in-vitro test. For the first time, 3D roughness parameters of the surface have been used to report the roughness of degraded sample. Additionally, values of the profile parameters including maximum peak height (R_p) and maximum valley depth (R_v) as well as surface parameters including the reduced core peak (S_{pk}) and the reduced core valley (S_{vk}) are given in Table 4. The samples immersed in CHBS, MHBS and NCS have almost the same profile and have both peaks and valleys relatively evenly distributed with a maximum S_{pk} of 1.4 µm for the sample immersed in MHBS and S_{vk} of 2.2 µm for the sample immersed in CHBS. The average area roughness (S_a) of the samples immersed in CHBS, MHBS and NCS are 2.4, 1.9 and 3.3 µm, respectively, which is higher than that of as received sample (~0.24 µm).

The analysis of the images for the samples immersed in DPBS and APBS suggests that particulates are formed over the surfaces. It has been demonstrated earlier that the size of the particles evolves with incorporation of protein into the solution, giving rise to a structure composed of small diameter particles with S_{pk} of 6.9 µm for the sample immersed in APBS as compare to that of 11.3 µm for the sample immersed in DPBS, while having almost the same S_{vk} of 1.1 µm.

Additionally, the effect of environment ions concentration and composition in the electrochemical interaction of iron with media is also defined by measurements of the open-circuit potential (OCP) of the immersed sample in the solutions (Table 4). According to these results, the OCP value for the pure iron sample was depended upon the solution composition. The

phosphate buffer solutions exhibited more positive potential (~ -550 mV), whereas the Hanks' solutions have more negative potentials (~ -750 mV). The presence of various species at the metal-solution interface could govern these differences.

Discussion

Body fluids are aqueous solutions consisting of organic and inorganic compounds and ions; complex interactions between the fluid and the host material affect the behaviour of metallic resorbable metal implant surface and the formation of degradation products. Hanks' and phosphate buffered (PBS) solutions are among the most common ones to conduct in-vitro tests. The degradation patterns of metals in these solutions can be used to a certain extent to predict the in-vivo behaviour of resorbable metals because the medium ion concentration is similar to the blood plasma one (Table 1).

Degradation of metals is a surface phenomenon dependent on the environment temperature, pH and solubility of metallic ions released from the surface, as well as chemical composition and ion concentration of the used medium. Pure iron is a chemically reactive metal which dissolves in aqueous solutions through the following electrochemical reactions:

Anodic reaction: $Fe \rightarrow Fe^{2+}+2e^{-}$ Eq. 3

Cathodic reaction: $O_2+2H_2O+4e^{-} \rightarrow 4OH^{-}$ Eq. 4

Overall reaction: $2Fe+O_2+2H_2O \leftrightarrow 2Fe(OH)_2$ Eq. 5

Iron (II) hydroxide is further oxidized by oxygen:

$Fe(OH)_2+1/2\,O_2+H_2O \rightarrow 2Fe(OH)_3$ Eq. 6

As pH increases, the local H^+ concentration at the metal-solution interface decreases faster than in the bulk solution that causes the formation of iron oxide/hydroxide over the pure iron surface according to the Pourbaix diagram (Fig. 4) for pure iron in water at 25 °C.[24] In this diagram, the concentration of dissolved iron ions is 10^{-6} mol·L^{-1} and $Fe(OH)_2$ and $Fe(OH)_3$ were considered as solid phases with a negligible solubility product (respectively Ksp $(Fe(OH)_2)= 8\times10^{-16}$ and Ksp $(Fe(OH)_3)= 4\times10^{-38}$).[25] However, these compounds, despite their thermodynamical stability in the considered conditions, do not have a protective nature because of their structure and the presence of crystalline defects.[26] Under the influence of environmental parameters, e.g. presence of hydrogen carbonates/bicarbonates and phosphates, chloride ions and changes in the concentration of corrosion products, the stability limits of each phase or chemical species in the already shown Pourbaix diagram are modified; furthermore, other ferrous compounds can form.

In this work, a complex interaction between pure iron, different kinds of ions and chemical species was studied; these interactions are also found in biomineralization patterns and geochemical processes.[27, 28] For instance, Génin *et al.* investigated the Pourbaix diagram of iron in the presence of chloride, carbonate and sulfate anions for different iron ion concentrations.[27] These ions are responsible for the formation of phases constituting an intermediate step in iron oxidation process: $Fe_6(OH)_{12}CO_3$, $Fe_4(OH)_8Cl$ and $Fe_6(OH)_{12}SO_4$ complexes, known as green rust (GR), formed in an aqueous environment. In a relatively wide pH range (7 < pH < 9), GRs form at the metallic interface that it plays a significant role in the degradation of iron-based alloys.[27] They dissolved when the oxidation reactions take place and they precipitates into ferric oxyhydroxides.[27] By the Pourbaix diagram and solubility of ferrous oxide at pH ≈ 7.4, the dissolution rate of pure iron is higher than its passivation one: this process further increases the release of iron ions in the media and promotes a faster oxidation of $Fe(OH)_2$.

The equilibrium equations for the iron ions with other ions and chemical species are listed in Table 5.[19, 22, 23, 27, 29-32] At the metal/solution interface, for a pH of 7.4, Fe_2^+ OH^-, Cl^-, $H_2PO_4^-$ /HPO_4^{2-} and HCO_3^{2-} ions are present. Noteworthy, GRs are prone to rapid oxidation and rapidly transformed into more stable compounds, such as α-FeOOH, γ-FeOOH or Fe_3O_4. The exposition to the atmosphere of the degraded surface formed during immersion in solution can also affect the whole degradation pattern of iron, by promoting and modifying the formation of chemical species that are not the same as those found in in-vivo mimicking experiments.

On the other hand, the 5% vol. CO_2 atmosphere at pH = 7.4 leads to the formation of H_2CO_3. It dissociates and forms bicarbonate and hydrogen carbonate ions, and finally, it leads to the deposition of $FeCO_3$. No carbonates were found on the surface of the studied samples. In fact, $FeCO_3$ is not thermodynamically stable for the conditions used in this work, and it does not form a passive protection layer.[19] The compaction of iron carbonate layer hinders the replenishment of protons at the iron surface; therefore, a higher local pH can be achieved.[31]

In general, microscopic observations indicate that the surface morphology of the degraded surfaces is grain orientation-dependent. Iron degradation produces rough surfaces, whose features are different for grains with different orientations. For pure iron, a higher dissolution rate is associated to {111} oriented surfaces.[33] Subsequently, the amount of dissolved iron varies and then modifies the local pH that leads to different local dissolution rates. Specific features, similar to triangular-base pyramids of various sizes, with an average height of a few hundred nanometres, are evident for some grains (Fig. 3); this particular topography is associated to {111} oriented surfaces. The roughness of {111} oriented grains is higher than that one for grains with other orientations, as previously mentioned. During in-vitro tests, selective grain orientation-dependent dissolution behaviour results in the retraction of more grains in {011} and {111} orientations. However, it is notable that the grain orientation contribution to the degradation rate of a polycrystalline material is marginal.[34]

A higher concentration of chloride ions in the solution promotes higher corrosion rates, thus forming a surface with a higher roughness indicator value. XPS measurements for degradation layer formed in samples immersed in low phosphate concentration solutions also show the incorporation of substantial amounts of chlorides. The detailed mechanism governing degradation behavior of pure iron in each particular media is explained as follows:

1) NCS (OCP of -600 mV): The higher iron amount on the surface of NCS samples compared to CHBS and MHBS ones is likely the result of the presence of a porous oxide layer. The formation of Fe_3O_4 can be due to the dissolution of $Fe(OH)_2$ or the oxidation of γ-FeOOH from the intermediate green rust formed by $Fe(OH)_2$ at pH < 7.4. This oxide layer, without any evidence of ferrous hydroxide formation on the surface of samples immersed in NCS, can be formed by the oxidation processes triggered by the simultaneous and conflicting effects of bicarbonates and chloride ions. The former are responsible for the formation of a passive layer while the latter affects iron degradation since they are responsible for local acidification. The sample surface is not covered by degradation products, because iron dissolved in solution form oxides and hydroxides, after the formation of carbonates.

2) CHBS (OCP of -650 mV, solution with the highest chloride concentration): The absence of evidence of degradation products in microscopy observation could be an indicative of no acquired passivation. For this reason, the corrosion process caused by the presence of chloride ion is predominant compared to the passivation one triggered by the presence of bicarbonate and carbonate ions. The final degradation product is mainly γ-FeOOH. Since the layer formed by degradation products does not cover homogeneously the surface, a higher concentration of chloride ions is attained at preferential sites, where the passive layer is not present. The formed metal chloride is then hydrolysed by water and forms hydroxide and free acid, lowering the pH value locally. This autocatalytic reaction leads to the growth of wider and deeper pits. A higher amount of chloride ions at the surface of CHBS samples can be responsible for a rougher topography (formation of wide valleys and high peaks, with a S_{vk} of about 2.2 µm for CHBS) than for MHBS ones. The presence of chloride ions can also affect the average thickness of oxide film (as confirmed by XPS), possibly by decreasing the passivation effect attributed to hydrogen carbonate and carbonate ions.[35] The chloride ion effect was already discussed by Maurice & Marcus.[36] It inhibits the coalescence and crystallization of a homogeneous and compact passive films and thus less resistant to dissolution. Marcus *et al.* studied the mechanism governing the breakdown of passive nanostructured films on metals in the presence of chloride ions.[37] Models of passive layers, breakdown and initiation of localized corrosion most often consider the film as a uniform, homogeneous and amorphous coating that hinders the transfer of cations from the metal surface to the electrolyte. Throughout their research, a complex model of passivity breakdown for the nanocrystalline grain barrier layer has been proposed. The model emphasizes three simultaneous mechanisms of (i) local thinning and dissolution of the oxide layer, (ii) metal voiding or (iii) particle growth at the metal/oxide interface followed by rupture of the barrier layer.[37]

3) MHBS (OCP of -750 mV, the solution with the highest bicarbonate concentration): A thicker layer of degradation product can be formed probably through oxidation of carbonate green rust to a more stable γ-FeOOH. The presence of a higher amount of γ-FeOOH in the loosed degradation products for this solution can be attributed to the different solubility constant of the degradation products which is in the following order: $Ksp_{\beta\text{-FeOOH}} > Ksp_{\gamma\text{-FeOOH}} >> Ksp_{\alpha\text{-FeOOH}}$. Borch *et al.* also report that the amount of iron dissolved in the solution will also modify the phase composition of the products.[38] Magnetite and γ-FeOOH are formed at high concentrations of ferrous iron (as for the sample immersed in MHBS) while α-FeOOH is formed for higher concentrations of carbonate and bicarbonates. As discussed earlier, the influence of chloride ions on the passivity breakdown of steel can cause a balance between two processes competing on the metal surface: stabilization of the passive film by carbonate and OH^- adsorption and disruption of the film by Cl^- adsorption.

In most studies focusing on the degradation of metals, the degradation phenomena are considered homogeneous, which is not the reality for polycrystalline metallic materials. Degradation layers of iron and iron-based alloys have often a multilayer structure, usually comprising an inner oxide layer covered by a lower density and less homogeneous outer layer mostly composed of ferrous hydroxides, the former being the barrier layer against cation exchange and the latter being an active layer, as described by Hermawan *et al*.[8]

4) DPBS (OCP of -600 mV, solution with the highest phosphates concentration): samples immersed in PBS and APBS did not form any crystalline iron oxide/hydroxide phase. Other authors already showed that the presence of phosphates/hydrogen phosphate/dihydrogen phosphate in solution favor iron passivation, promoting the formation of phosphates amorphous in its amorphous or crystalline form (vivianite, crystalline iron phosphate) and green rust.[38] Refait *et al.* proposed that the amorphous layer created at the iron surface consist of nanoparticles showing a structure similar to that of carbonate-based GR; these single nanoparticles are embedded in a matrix of amorphous adsorbed phosphate species.[39] The adsorption of phosphate species is supposed to prevent the growth and ripening of such nanoparticles into a full carbonate GR. These results can be interpreted by considering the way phosphate species interact with iron species depending on parameters such as pH, dissolved iron and phosphate concentrations, and dissolved O_2 concentration. Phosphate species can interact strongly with iron hydroxides: FeOOH species adsorb iron ions on their surface, which can trigger the precipitation of fine iron phosphate species. The iron phosphates are in fact characterized a very low solubility (for instance, log Ksp = −35.77 at 25 °C for vivianite).[25]

The EDS analyses clearly show the incorporation of phosphates in the surface passive layer. The ferrous phosphate film was formed by diffusion of iron ions from the material bulk toward the liquid/solid interface, whereas phosphorus and oxygen diffuse in the opposite direction.[40] The outer phosphate layer could hinder oxygen diffusion and further oxidation at the metal–layer interface.

When the amount of phosphate ions, to promote ferrous phosphate precipitation, is higher than the chloride ion one, responsible for metal dissolution, pitting is clearly inhibited.[41] Furthermore, Mao *et al.* reported that Fe(II)-phosphate species

play a significant role in Fe(II) oxidation in NaCl-HCO_3^- buffer solutions with different concentrations of phosphate ions, for $6.0 \leq pH \leq 7.8$.[42] Here, it revealed that the present of phosphate, chloride and bicarbonate ions in solution conquered a more positive OCP.

5) APBS (OCP of -550 mV, solution with albumin): the formation of crystalline phases, similarly to the DPBS case, is not evident even if some albumin is dissolved in the medium. The competitive adsorption between organic compounds and different cations and anions of the near surface of samples can explain the inhibition of the degradation by proteins thus suppressing the dissolution of iron.[43] In a recent work, Hedberg et al.[44] reported that at the protein-solution interfaces, the bulk pH is quite different compared to a pH near a protein surface. Moreover, the concentration of Na^+ at the stainless steel surface is higher compared with the bulk solution whereas the concentration of chloride ions is shortened. The presence of some organic compounds (albumin) played the role of nucleation inhibitor in the precipitation process. In another work, it is reported that the presence of proteins affected the crystallinity and the shape of the phosphate aggregates on the surface, the addition of proteins retards the crystallization of calcium phosphate.[23]

Conclusions

The presence versus absence of different biological ions and proteins has a considerable effect on iron degradation behavior. Microscopic studies revealed an inhomogeneous film growth which is attributed to different local dissolution-passivation behavior in the iron sample. Furthermore, in-situ investigation of iron degradation is needed for evaluation of the original composition of intermediate oxidation products.

The result of this work demonstrated that chloride ions in a CO_2-rich atmosphere can induce pitting corrosion and a porous surface. Its degradation has been shown to proceed to a mixture of magnetite, α-FeOOH and γ -FeOOH, via initial formation of carbonate green rust. Bicarbonate ions are observed to stimulate the corrosion of iron during the early immersion stage. In the presence of phosphates, the degradation inhibited, and the formation of pitting corrosion is significantly delayed due to precipitation of iron phosphate. It was evident that samples immersed in phosphate buffer solutions were initially covered by the formation of hydrated iron phosphate. The presence of proteins led to the formation of a relatively poor crystalline (amorphous) layer; this surface passivation layer results from the fast precipitation of iron carbonate susceptible to subsequently hinder pitting corrosion. Variation of potential should also be considered besides concentration of chemical species.

These results improve our understanding of the degradation mechanism of pure iron in the complex physiological environment. In-vitro degradation of pure iron is a function of following factors (i) composition of the electrolyte solution, (ii) quality of degradation layer, pore and defect density and (iii) local dissolution and pH which could be explained by the formation and dissolution of salt film coupled to changes in local pH. The contact between the material surface and the host tissue involved in the implantation must be carefully considered while assessing iron and iron-based alloys in-vitro for any medical application. Mainly because the degradation behavior of pure iron is solution-dependent, the overall result of the current work stress the importance of conducting in-vitro static immersion test in multiple solutions simultaneously. This approach could represent a reliable testing procedure for performance assessment of developing metallic resorbable medical devices.

Acknowledgements

This research was partially funded by the Natural Science and Engineering Research Council of Canada, Canadian Institute for Health Research. JH was an undergraduate student supported by the Natural Sciences and Engineering Research Council of Canada Undergraduate Student Research Award (NSERC-USRA).

References

1. H. Hermawan, D. Dubé and D. Mantovani, *Acta biomaterialia*, 2010, **6**, 1693-1697.
2. A. Purnama, H. Hermawan and D. Mantovani, *Journal of Biomaterials and Tissue Engineering*, 2014, **4**, 868-874.
3. R. Waksman, R. Pakala, R. Baffour, R. Seabron, D. Hellinga and F. O. Tio, *Journal of interventional cardiology*, 2008, **21**, 15-20.
4. M. Peuster, C. Hesse, T. Schloo, C. Fink, P. Beerbaum and C. von Schnakenburg, *Biomaterials*, 2006, **27**, 4955-4962.
5. T. Kraus, F. Moszner, S. Fischerauer, M. Fiedler, E. Martinelli, J. Eichler, F. Witte, E. Willbold, M. Schinhammer and M. Meischel, *Acta biomaterialia*, 2014, **10**, 3346-3353.
6. D. Pierson, J. Edick, A. Tauscher, E. Pokorney, P. Bowen, J. Gelbaugh, J. Stinson, H. Getty, C. H. Lee, J. Drelich and J. Goldman, *Journal of Biomedical Materials Research Part B: Applied Biomaterials*, 2012, **100B**, 58-67.
7. H. Hermawan, D. Dubé and D. Mantovani, *Journal of Biomedical Materials Research Part A*, 2010, **93**, 1-11.
8. H. Hermawan, A. Purnama, D. Dube, J. Couet and D. Mantovani, *Acta biomaterialia*, 2010, **6**, 1852-1860.
9. M. Moravej, A. Purnama, M. Fiset, J. Couet and D. Mantovani, *Acta biomaterialia*, 2010, **6**, 1843-1851.
10. A. Francis, Y. Yang, S. Virtanen and A. Boccaccini, *Journal of Materials Science: Materials in Medicine*, 2015, **26**, 1-16.
11. M. Schinhammer, A. C. Hänzi, J. F. Löffler and P. J. Uggowitzer, *Acta biomaterialia*, 2010, **6**, 1705-1713.
12. T. Huang, J. Cheng, D. Bian and Y. Zheng, *Journal of Biomedical Materials Research Part B: Applied Biomaterials*, 2015.

13. J. Kundrak, K. Gyani and V. Bana, *The International Journal Of Advanced Manufacturing Technology*, 2008, **38**, 110-119.
14. M. Hadnadjev, T. Vulic, R. Marinkovic-Neducin, Y. Suchorski and H. Weiss, *Applied Surface Science*, 2008, **254**, 4297-4302.
15. R. Heuberger, A. Rossi and N. D. Spencer, *Lubrication Science*, 2008, **20**, 79-102.
16. T. Daou, S. Begin-Colin, J. Greneche, F. Thomas, A. Derory, P. Bernhardt, P. Legaré and G. Pourroy, *Chemistry of Materials*, 2007, **19**, 4494-4505.
17. A. Hermas, M. Nakayama and K. Ogura, *Electrochimica Acta*, 2005, **50**, 3640-3647.
18. H. Mazor, D. Golodnitsky, L. Burstein, A. Gladkich and E. Peled, *Journal of Power Sources*, 2012, **198**, 264-272.
19. J. Heuer and J. Stubbins, *Corrosion Science*, 1999, **41**, 1231-1243.
20. S. Guo, L. Xu, L. Zhang, W. Chang and M. Lu, *Corrosion Science*, 2012, **63**, 246-258.
21. M. C. Biesinger, B. P. Payne, A. P. Grosvenor, L. W. Lau, A. R. Gerson and R. S. C. Smart, *Applied Surface Science*, 2011, **257**, 2717-2730.
22. H. Tsuge, Y. Tanaka, S. Yoshizawa and T. Kuraishi, *Chemical Engineering Research and Design*, 2002, **80**, 105-110.
23. K. Wang, Y. Leng, X. Lu, F. Ren, X. Ge and Y. Ding, *CrystEngComm*, 2012, **14**, 5870-5878.
24. A. Jain, S. P. Ong, G. Hautier, W. Chen, W. D. Richards, S. Dacek, S. Cholia, D. Gunter, D. Skinner and G. Ceder, *APL Materials*, 2013, **1**, 011002.
25. M. Reffass, R. Sabot, M. Jeannin, C. Berziou and P. Refait, *Electrochimica Acta*, 2009, **54**, 4389-4396.
26. R. R. Hussain and T. Ishida, *Int. J. Electrochem. Sci*, 2009, **4**, 1178-1195.
27. J.-M. R. Génin, C. Ruby, A. Géhin and P. Refait, *Comptes Rendus Geoscience*, 2006, **338**, 433-446.
28. C. Ruby, M. Abdelmoula, S. Naille, A. Renard, V. Khare, G. Ona-Nguema, G. Morin and J.-M. R. Génin, *Geochimica et Cosmochimica Acta*, 2010, **74**, 953-966.
29. F. F. Eliyan and A. Alfantazi, *Corrosion*, 2014, **70**, 880-898.
30. E. Abelev, T. Ramanarayanan and S. Bernasek, *Journal of The Electrochemical Society*, 2009, **156**, C331-C339.
31. J. Han, D. Young, H. Colijn, A. Tripathi and S. Nešić, *Industrial & Engineering Chemistry Research*, 2009, **48**, 6296-6302.
32. I. Azoulay, C. Rémazeilles and P. Refait, *Corrosion Science*, 2012, **58**, 229-236.
33. A. Schreiber, J. Schultze, M. Lohrengel, F. Kármán and E. Kálmán, *Electrochimica Acta*, 2006, **51**, 2625-2630.
34. C. S. Obayi, R. Tolouei, C. Paternoster, S. Turgeon, B. A. Okorie, D. O. Obikwelu, G. Cassar, J. Buhagiar and D. Mantovani, *Acta biomaterialia*, 2015, **17**, 68-77.
35. P. Ghods, O. Isgor, J. Brown, F. Bensebaa and D. Kingston, *Applied Surface Science*, 2011, **257**, 4669-4677.
36. V. Maurice and P. Marcus, in *Progress in Corrosion Science and Engineering I*, Springer, 2010, pp. 1-58.
37. P. Marcus, V. Maurice and H.-H. Strehblow, *Corrosion Science*, 2008, **50**, 2698-2704.
38. T. Borch, Y. Masue, R. K. Kukkadapu and S. Fendorf, *Environmental science & technology*, 2007, **41**, 166-172.
39. P. Refait, M. Reffass, J. Landoulsi, R. Sabot and M. Jeannin, *Colloids and Surfaces A: Physicochemical and Engineering Aspects*, 2007, **299**, 29-37.
40. C. Giacomelli and A. Spinelli, *Anti-Corrosion Methods and Materials*, 2004, **51**, 189-199.
41. L. Yohai, M. Vázquez and M. Valcarce, *Electrochimica Acta*, 2013, **102**, 88-96.
42. Y. Mao, A. N. Pham, A. L. Rose and T. D. Waite, *Geochimica et Cosmochimica Acta*, 2011, **75**, 4601-4610.
43. H. Amar, J. Benzakour, A. Derja, D. Villemin and B. Moreau, *Journal of electroanalytical chemistry*, 2003, **558**, 131-139.
44. Y. Hedberg, X. Wang, J. Hedberg, M. Lundin, E. Blomberg and I. O. Wallinder, *Journal of Materials Science: Materials in Medicine*, 2013, **24**, 1015-1033.

List of Tables

Table 1

Ion(s) (mg/L)	Blood plasma [14]	NCS	CHBS	MHBS	DPBS	APBS
Na^+	3000 – 3400	5425	3258	2795	3519	3519
K^+	130 – 210	-	227	172	162	162
Cl^-	3400 – 3750	3518	5043	3542	4947	4947
HCO^{3-}	1100 – 2400	-	254	1654	-	-
$H2PO^{4-}/HPO_4^{2-}$	270 – 450	-	75	48	920	920
Ca^{2+}	84 – 110	-	-	35	-	-
Mg^{2+}	15 – 30	-	-	14	-	-
SO_4^{2-}	5 – 15	-	-	78	-	-
D-Glucose	600 – 1100	-	1000	720	-	-
Albumin	35000-50000	-	-	-	-	1000

Table 2.

	Fe-O	Fe-OH	Fe-PO_4	Fe-CO_3	H_2O	Hydrocarbon
O1s	529.9[14]	531.3[15]	531.7[16]	531.9[17]	532.4 [15]	
	530.0[18]	531.6[15]	532.0[18]	531.9[19]	532.8[15]	
	530.1[20]	531.0[20]	532.0[20]	533.7[20]	532.1[20]	
C1s				289.4[17]		284.6[17]
				289.4[19]		284.8[19]

Table 3.

O1s (at .%)	AR	NCS	CHBS	MHBS	DPBS	APBS
O1s (1)	48.6	51.5	32.9	37.1	6.8	2.2
O1s (2)	41.4	33.7	60.0	50.4	74.7	89.6
O1s (3)	9.9	11.6	7.0	12.4	18.4	8.1
Iron-oxide (at .%)	21.9	29.8	17.2	19.8	3.8	0.9
Iron-Hydroxide/Phosphate (at .%)	18.7	19.5	31.3	26.9	42.3	38.1
Oxide:Hydroxide/Phosphate	1.17	1.50	0.55	0.74	0.09	0.02

Table 4.

Material	2D R_q (µm)	2D R_p (µm)	2D R_v (µm)	3D S_q (µm)	3D S_{pk} (µm)	3D S_{vk} (µm)	OCP (-mV)
NCS	1.5	11.0	-8.2	3.3	1.3	2.1	600
CHBS	1.2	9.1	-5.7	2.4	1.0	2.2	650
MHBS	1.0	13.3	-3.8	1.9	1.4	1.6	750
DPBS	3.2	23.0	-7.8	5.2	6.9	1.1	600
APBS	5.0	29.0	-7.3	6.5	11.3	1.1	550

Table 5.

Ion in medium	Reactions	Ref
HCO^{3-}	$CO_{2\,(g)} \leftrightarrow CO_{2\,(aq)}+H_2O \rightarrow H_2CO_3 \overset{pH=7.4}{\longleftrightarrow} H^+ + HCO_3^-$ $6Fe+HCO_3^-+12H_2O \leftrightarrow Fe_6(OH)_{12}CO_3+13H^++14e^-$ $6Fe^{2+}+HCO_3^-+12H_2O \leftrightarrow Fe_6(OH)_{12}CO_3+13H^++2e^-$ $6FeOH^++HCO_3^-+6H_2O \leftrightarrow Fe_6(OH)_{12}CO_3+7H^++2e^-$ $Fe_6(OH)_{12}CO_3 \leftrightarrow 6\alpha\text{-}FeOOH+CO_3^{-2}+6H^++4e^-$ $HCO_3^- \leftrightarrow CO_3^{2-}+H^+$ $Fe^{2+}+CO_3^{2-} \leftrightarrow FeCO_3$ $FeCO_3 \rightarrow FeO+CO_2$ $FeO+O_2 \rightarrow 2Fe_2O_3$ $FeO+H_2O \rightarrow Fe_3O_4+H_2$ $7Fe(OH)_2+2CO_3^{2-}+H_2O \rightarrow 4Fe(OH)_2.2Fe(OH)_3CO_3+H_2+2OH^-$ $4Fe(OH)_2.2Fe(OH)_3CO_3+4H^+ \rightarrow Fe_3O_4+3Fe^{2+}+CO_3^{2-}+8H_2O$	14 15 21
Cl^-	$Fe^{2+}+2Cl^- \leftrightarrow FeCl_2+H_2O \leftrightarrow Fe(OH)_2+HCl$ $4Fe+Cl^-+8H_2O \leftrightarrow Fe_4(OH)_8Cl+8H^++9e^-$ $4Fe^{2+}+Cl^-+8H_2O \leftrightarrow Fe_4(OH)_8Cl+8H^++e^-$ $4FeOH^++Cl^-+4H_2O \leftrightarrow Fe_4(OH)_8Cl+4H^++e^-$ $Fe_4(OH)_8Cl \leftrightarrow 4\gamma\text{-}FeOOH+Cl^-+4H^++3e^-$ $\gamma\text{-}FeOOH \overset{dry}{\rightarrow} Fe_3O_4$ $\gamma\text{-}FeOOH \rightarrow Fe(III) \rightarrow \alpha\text{-}FeOOH$	19 22 23 24 25
HPO_4^- /HPO_4^{2-}	$3Fe^{2+}+2H_2PO_4^-4+8H_2O \leftrightarrow Fe_3(PO_4)_2+2H^+$ $Fe+2H_2PO_4^- \leftrightarrow Fe(H_2PO_4)_2+2e^-$ $3Fe(H_2PO_4)_2 \leftrightarrow Fe_3(PO_4)_2+4H_3PO_4$ $3Fe+2HPO_4^{2-} \leftrightarrow Fe_3(PO_4)_2+2H^++6e^-$ $Fe_3(PO_4)_2+6H_2O \leftrightarrow 3\gamma\text{-}FeOOH+2HPO_4^{2-}+7H^++3e^-$ $Fe_3(PO_4)_2+4H_2O \leftrightarrow Fe_3O_4+2HPO_4^{2-}+6H^++2e^-$	19

Table 5.(as an image)

Ion in medium	Reactions	Ref
HCO^{3-}	$CO_{2\,(g)} \leftrightarrow CO_{2\,(aq)}+H_2O \rightarrow H_2CO_3 \overset{pH=7.4}{\longleftrightarrow} H^+ + HCO_3^-$	14 15 21
	$6Fe+HCO_3^-+12H_2O \leftrightarrow Fe_6(OH)_{12}CO_3+13H^++14e^-$	
	$6Fe^{2+}+HCO_3^-+12H_2O \leftrightarrow Fe_6(OH)_{12}CO_3+13H^++2e^-$	
	$6FeOH^++HCO_3^-+6H_2O \leftrightarrow Fe_6(OH)_{12}CO_3+7H^++2e^-$	
	$Fe_6(OH)_{12}CO_3 \leftrightarrow 6\alpha\text{-}FeOOH+CO_3^{-2}+6H^++4e^-$	
	$HCO_3^- \leftrightarrow CO_3^{2-}+H^+$	
	$Fe^{2+}+CO_3^{2-} \leftrightarrow FeCO_3$	
	$FeCO_3 \rightarrow FeO+CO_2$	
	$FeO+O_2 \rightarrow 2Fe_2O_3$	
	$FeO+H_2O \rightarrow Fe_3O_4+H_2$	
	$7Fe(OH)_2+2CO_3^{2-}+H_2O \rightarrow 4Fe(OH)_2.2Fe(OH)_3CO_3+H_2+2OH^-$	
	$4Fe(OH)_2.2Fe(OH)_3CO_3+4H^+ \rightarrow Fe_3O_4+3Fe^{2+}+CO_3^{2-}+8H_2O$	
Cl^-	$Fe^{2+}+2Cl^- \leftrightarrow FeCl_2+H_2O \leftrightarrow Fe(OH)_2+HCl$	19 22 23 24 25
	$4Fe+Cl^-+8H_2O \leftrightarrow Fe_4(OH)_8Cl+8H^++9e^-$	
	$4Fe^{2+}+Cl^-+8H_2O \leftrightarrow Fe_4(OH)_8Cl+8H^++e^-$	
	$4FeOH^++Cl^-+4H_2O \leftrightarrow Fe_4(OH)_8Cl+4H^++e^-$	
	$Fe_4(OH)_8Cl \leftrightarrow 4\gamma\text{-}FeOOH+Cl^-+4H^++3e^-$	
	$\gamma\text{-}FeOOH \overset{dry}{\rightarrow} Fe_3O_4$	
	$\gamma\text{-}FeOOH \rightarrow Fe(III) \rightarrow \alpha\text{-}FeOOH$	
HPO_4^- /HPO_4^{2-}	$3Fe^{2+}+2H_2PO_4^-4+8H_2O \leftrightarrow Fe_3(PO_4)_2+2H^+$	19
	$Fe+2H_2PO_4^- \leftrightarrow Fe(H_2PO_4)_2+2e^-$	
	$3Fe(H_2PO_4)_2 \leftrightarrow Fe_3(PO_4)_2+4H_3PO_4$	
	$3Fe+2HPO_4^{2-} \leftrightarrow Fe_3(PO_4)_2+2H^++6e^-$	
	$Fe_3(PO_4)_2+6H_2O \leftrightarrow 3\gamma\text{-}FeOOH+2HPO_4^{2-}+7H^++3e^-$	
	$Fe_3(PO_4)_2+4H_2O \leftrightarrow Fe_3O_4+2HPO_4^{2-}+6H^++2e^-$	

List of Figures

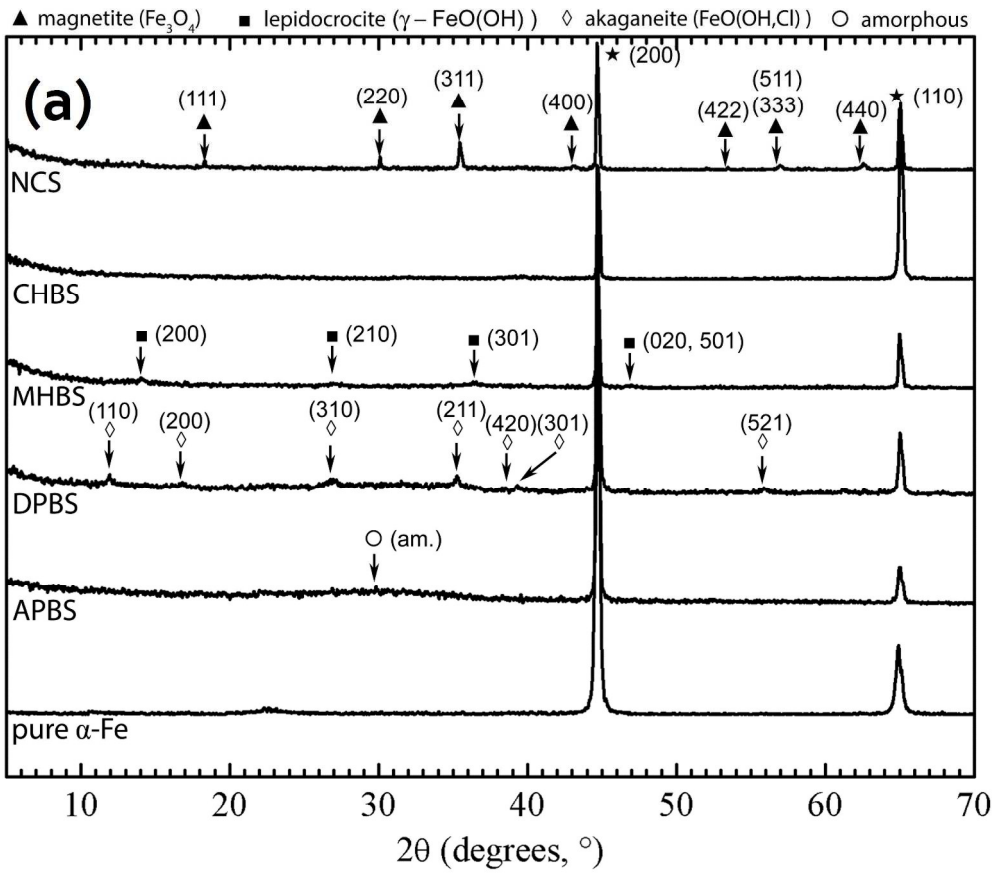

Figure 1. XRD patterns of (a) as received pure iron sample and samples after 14-day immersion in test solutions and (b) loosed degradation product settled at the bottom of the bottles during the 14-day in vitro test.
285x248mm (300 x 300 DPI)

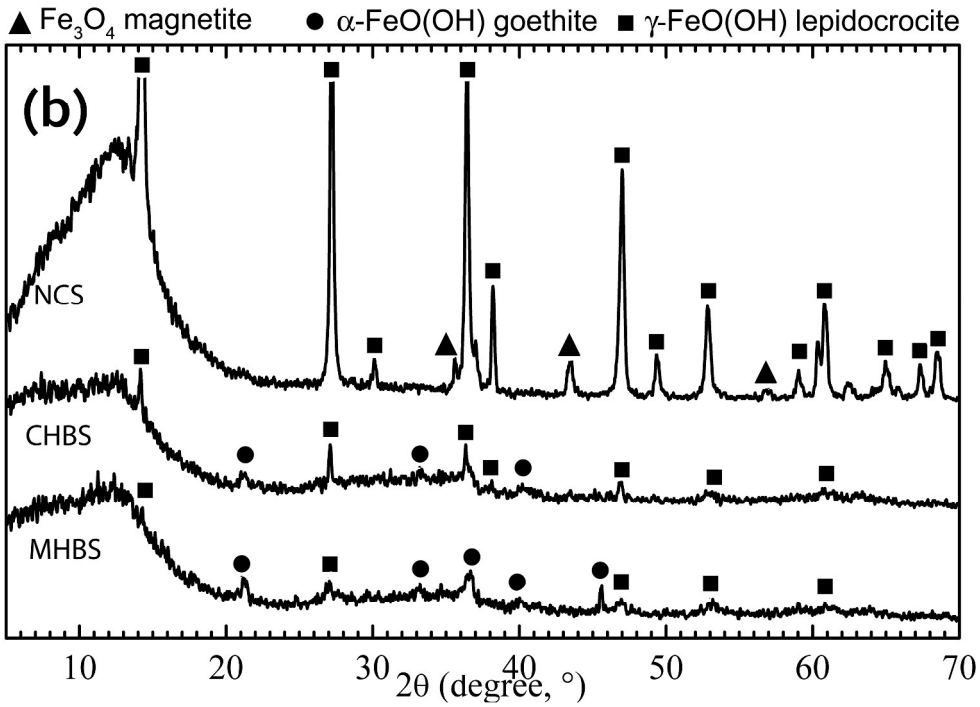

Figure 1. XRD patterns of (a) as received pure iron sample and samples after 14-day immersion in test solutions and (b) loosed degradation product settled at the bottom of the bottles during the 14-day in vitro test.
576x403mm (300 x 300 DPI)

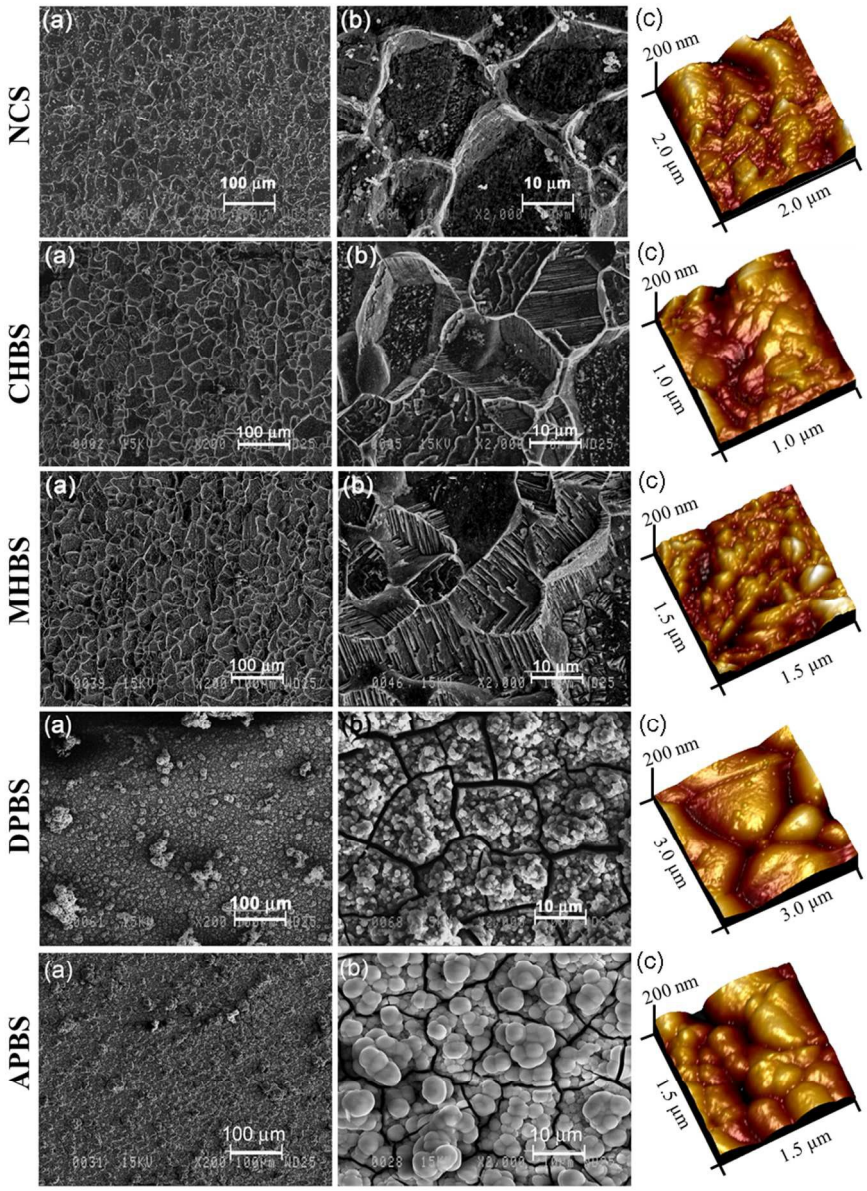

Figure 2. Microscopical images of sample surface after 14-day in vitro degradation test: (a) SEM general view of the surfaces ×200, (b) SEM higher magnification of degraded surfaces ×2000 and (c) AFM images of surfaces.
259x350mm (96 x 96 DPI)

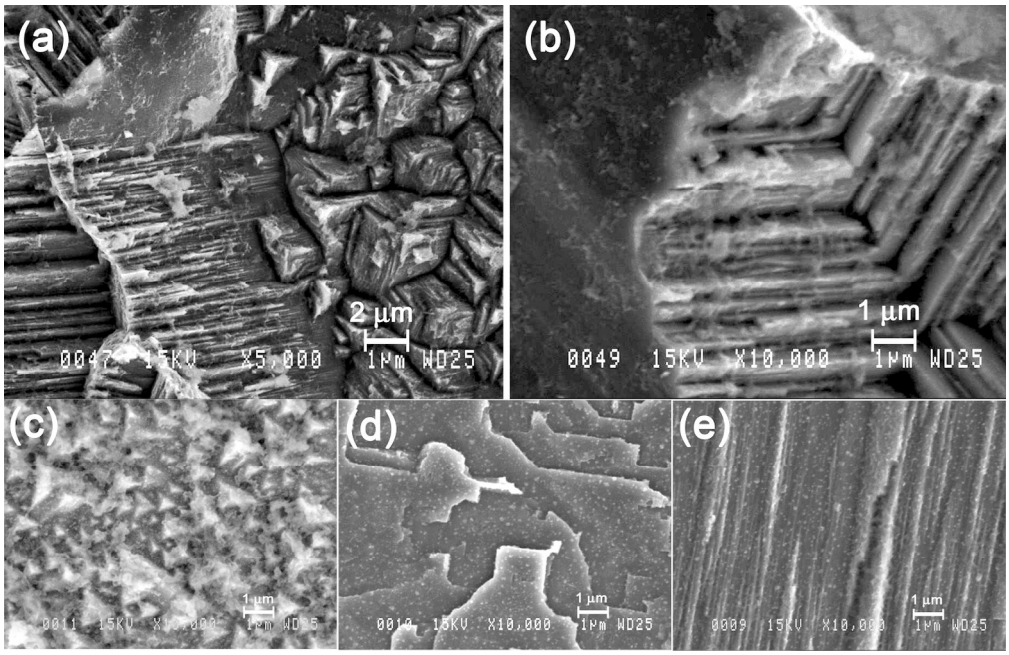

Figure 3. SEM images showing details of degraded sample surfaces immersed in (a,b) MHBS and (c-e) CHBS.
309x199mm (300 x 300 DPI)

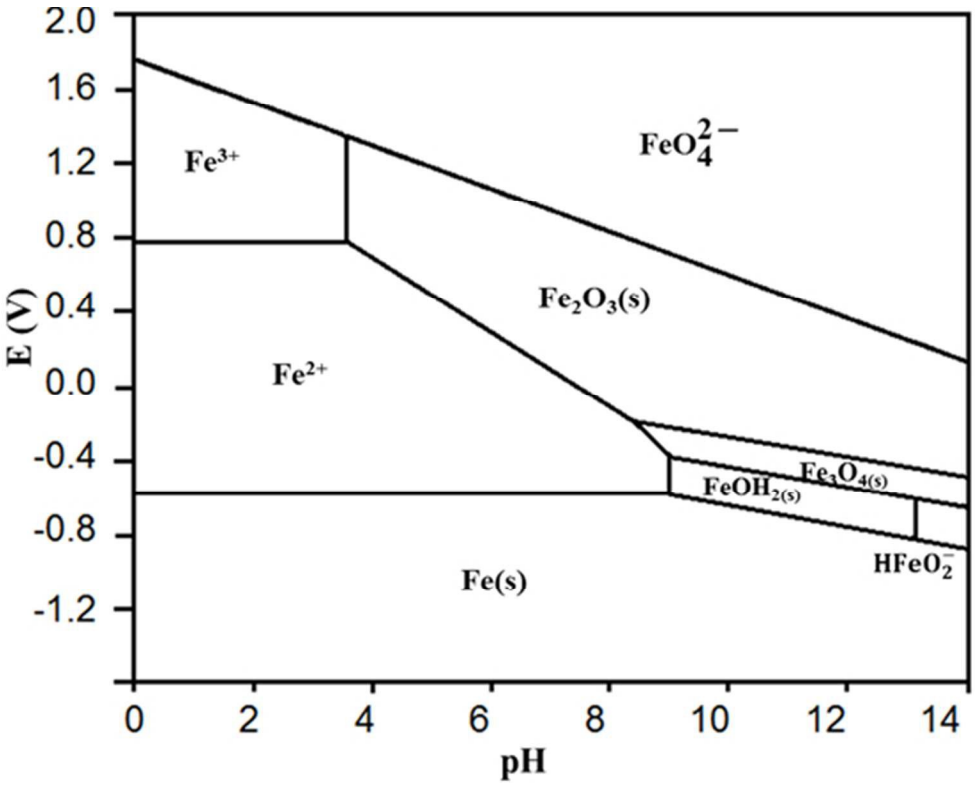

Figure 4. Simplified Potential-pH Pourbaix diagrams of iron compounds.
200x154mm (72 x 72 DPI)